ARTICLE　　**OPEN**

Re$_{1-x}$Mo$_x$ as an ideal test case of time-reversal symmetry breaking in unconventional superconductors

Tian Shang [1]✉, Christopher Baines[2], Lieh-Jeng Chang[3], Dariusz Jakub Gawryluk [1], Ekaterina Pomjakushina [1], Ming Shi[4], Marisa Medarde[1] and Toni Shiroka [2,5]✉

Non-centrosymmetric superconductors (NCSCs) are promising candidates in the search for unconventional and topological superconductivity. The α-Mn-type rhenium-based alloys represent excellent examples of NCSCs, where spontaneous magnetic fields, peculiar to time-reversal symmetry (TRS) breaking, have been shown to develop in the superconducting phase. By converse, TRS is preserved in many other isostructural NCSCs, thus leaving the key question about its origin fully open. Here, we consider the superconducting Re$_{1-x}$Mo$_x$ ($0 \leq x \leq 1$) family, which comprises both centro- and non-centrosymmetric structures and includes also two extra superconducting phases, β-CrFe and bcc-W. Muon-spin relaxation and rotation (μSR) measurements show a gradual increase of the relaxation rate below T_c, yet its independence of the crystal structure, suggesting that rhenium presence and its amount are among the key factors for the appearance and the extent of TRS breaking in the α-Mn-type NCSCs. The reported results propose Re$_{1-x}$Mo$_x$ as an ideal test case for investigating TRS breaking in unconventional superconductors.

npj Quantum Materials (2020)5:76 ; https://doi.org/10.1038/s41535-020-00279-1

INTRODUCTION

Superconductors with a centrosymmetric crystal structure can host spin-singlet- or spin-triplet states with a well-defined parity—even and odd, respectively. However, in non-centrosymmetric superconductors (NCSCs), these strict symmetry-imposed requirements are relaxed, thus implying the possibility of parity-mixed superconducting states. The recent interest in NCSCs is mostly related to their unconventional superconducting properties[1]. Because of the mixed superconducting pairing, NCSCs may display significantly different properties compared to their centrosymmetric counterparts, e.g., upper critical fields beyond the Pauli limit, nodes in the superconducting gaps, etc.[1]. Owing to the possibility of mixed singlet- and triplet pairings, NCSCs rank among the foremost categories of superconducting materials in which to look for topological superconductivity or to realize the Majorana fermions, offering potential applications as, for instance, quantum computing[2–9].

More intriguingly, some of the NCSCs also exhibit broken time-reversal symmetry (TRS) in the superconducting state[10], a manifestation of unconventional superconductivity. Among these, α-Mn-type ReTM (TM = Ti, Nb, Zr, and Hf) alloys represent one of the most interesting NCSC families. Widely studied by means of micro- and macroscopic techniques, they often break the time-reversal symmetry in the superconducting state[11–14]. A similar feature has also been discovered in centrosymmetric Sr$_2$RuO$_4$, PrOs$_4$Sb$_{12}$, and in pure rhenium[14–16]. Yet, TRS seems to be preserved in Mg$_{10}$Ir$_{19}$B$_{16}$, Nb$_{0.5}$Os$_{0.5}$, and Re$_3$W[17–19]. Since the latter three share the same α-Mn non-centrosymmetric structure with ReTM, this raises a very interesting fundamental question about the role of non-centrosymmetric structure in the appearance of TRS breaking in ReTM alloys. The best way to address this question consists in finding a family of compounds which exhibit crystal structures both with and without inversion symmetry, while still preserving the original stoichiometry.

Indeed, despite the plausibility of the above examples, they still refer to different materials (although some of them share similar structures). Depending on the synthesis protocol, Re$_3$W can adopt either an hcp-Mg-type (centrosymmetric) or an α-Mn-type (non-centrosymmetric) crystal structure, yet neither is found to break TRS below T_c[19]. On the other hand, many superconducting ReTM alloys, although known to break TRS, invariably adopt a single (α-Mn-type) structure[11–14]. In general, most ReTM phase diagrams are rather simple, with the superconducting cases being limited to the hcp-Mg- and α-Mn crystal structures. Clearly, the absence of an ideal test system leaves open the question of the origin of TRS breaking in the ReTM family and of its possible indirect link with the lack of space-inversion symmetry.

Unlike the above cases, the Re$_{1-x}$Mo$_x$ binary alloys reported here might represent such an ideal and rare candidate system. Indeed, depending on the synthesis protocol, compounds with different Re/Mo ratios can be either centrosymmetric or non-centrosymmetric while, most importantly, they all exhibit a superconducting state at low temperature[20]. In general, since the Re$_{1-x}$Mo$_x$ system remains largely unexplored at a deeper level, we conducted systematic microscopic investigations of its superconductivity via the muon-spin relaxation and rotation (μSR) method. This required the synthesis and the preliminary characterization of the magnetic, electrical, and thermodynamic properties of the full range of Re$_{1-x}$Mo$_x$ solid solution[20]. The μSR results presented here allow us not only to establish the presence of TRS breaking but also to quantify it. By correlating the extent of TRS breaking in the Re$_{1-x}$Mo$_x$ series to the Re-content we find that in ReTM materials the time-reversal symmetry breaking is most likely related to the Re content rather than to crystal structure.

[1]Laboratory for Multiscale Materials Experiments, Paul Scherrer Institut, CH-5232 Villigen PSI, Switzerland. [2]Laboratory for Muon-Spin Spectroscopy, Paul Scherrer Institut, CH-5232 Villigen PSI, Switzerland. [3]Department of Physics, National Cheng Kung University, Tainan 70101, Taiwan. [4]Swiss Light Source, Paul Scherrer Institut, CH-5232 Villigen PSI, Switzerland. [5]Laboratorium für Festkörperphysik, ETH Zürich, CH-8093 Zürich, Switzerland. ✉email: tian.shang@psi.ch; tshiroka@phys.ethz.ch

RESULTS

Rich structural- and superconducting phase diagram

According to diffraction- and physical-properties characterizations, binary $Re_{1-x}Mo_x$ alloys exhibit very rich structural- and superconducting phase diagrams. As shown in Fig. 1a, depending on Re/Mo concentration, different synthesis procedures can produce four different solid phases: hexagonal hcp-Mg ($P6_3/mmc$, No. 194), cubic α-Mn ($I\bar{4}3m$, No. 217), tetragonal β-CrFe ($P4_2/mnm$, No. 136), and cubic bcc-W ($Im\bar{3}m$, No. 229). Except for the non-centrosymmetric α-Mn, the other three structures are centrosymmetric. Their unit-cell crystal structures are shown schematically in Fig. 1b, while details such as the lattice parameters and the atomic coordinates are reported elsewhere[20]. Although $Re_{1-x}Mo_x$ alloys exhibit different crystal structures as x changes, they all become superconductors at low temperature. By increasing the Mo content, the superconducting transition temperature T_c varies non-monotonically, thus defining three distinct superconducting regions. The first superconducting region (achieved on the Re-rich side and with highest $T_c = 9.43$ K), corresponds to alloys adopting an hcp-Mg-type structure. For $x = 0.23$, both centrosymmetric (hcp-Mg) and non-centrosymmetric (α-Mn) crystal structures are obtained, the latter showing a T_c value about 1 K lower than the former. In the second superconducting region, where the alloys adopt a β-CrFe-type structure, the superconducting transition temperature $T_c \sim 6.3$ K is somewhat lower than in the other regions and almost independent of Mo content. Upon further increasing the Mo content, the third superconducting region shows up for $x > 0.5$. Here, all the samples display a cubic bcc-W-type structure and the highest T_c reaches 12.4 K (for $x = 0.6$). Close to the phase boundaries, the alloys show multiple superconducting transitions. To exclude possible extrinsic effects related to them, the μSR measurements were performed only on samples away from the phase boundaries.
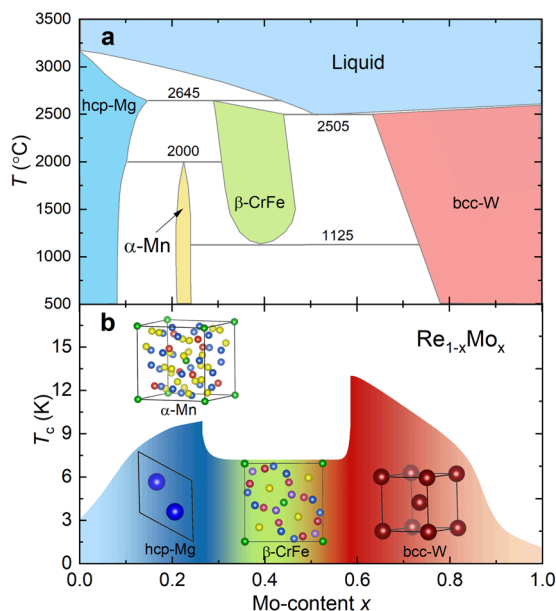

Fig. 1 Structural and superconducting phase diagram of $Re_{1-x}Mo_x$. **a** The phase diagram of the binary $Re_{1-x}Mo_x$ alloys includes four different solid phases, whose crystal structures are shown schematically in **b**. For $x = 0.23$, both centrosymmetric (hexagonal hcp-Mg) and non-centrosymmetric (cubic α-Mn) structures can be obtained. The details of the crystal structures can be found in Shang et al.[20]. **b** Superconducting transition temperatures T_c versus Mo content, as determined from electrical resistivity, magnetic susceptibility, and specific-heat measurements (see ref. [20]). Colors identify the various phases and highlight the correlation between the superconducting properties and crystal structures.

Zero field-μSR and evidence of time-reversal symmetry breaking

Owing to the large muon gyromagnetic ratio (851.615 MHz/T) and to the availability of 100% spin-polarized muon beams, the zero-field (ZF) μSR is a very sensitive method for detecting weak magnetic fields, down to ~0.01 mT[21]. Consequently, it has been successfully used to study the TRS breaking in the superconducting states of different types of superconductors[13–16,22–24], as well as in the search for unconventional superconductors with broken TRS[25,26].

The ZF-μSR measurements were performed in both the normal and the superconducting states of $Re_{1-x}Mo_x$ alloys, whose crystal structures cover the whole phase diagram. Representative ZF-μSR spectra for $Re_{1-x}Mo_x$, collected above and below T_c, are shown in Fig. 2a for $x = 0$ (i.e., pure rhenium) and in Fig. 2b for $x = 0.12$. The lack of any oscillations in the spectra, implies the non-magnetic nature of $Re_{1-x}Mo_x$. Consequently, in absence of external fields, the relaxation is mostly determined by the interaction of the muon spins with the randomly oriented nuclear magnetic moments in $Re_{1-x}Mo_x$. The rather fast decay of ZF-μSR asymmetry reflects the relatively large nuclear moment of rhenium (~3.2 μ_n). The ZF-μSR asymmetry could be described by means of a phenomenological relaxation function, consisting of a combination of Gaussian- and Lorentzian Kubo-Toyabe relaxations [see Eq. (1)]. The resulting Gaussian relaxation rates σ_{ZF} vs temperature for $x = 0$ and 0.12 are shown in Fig. 2c and d, respectively. In both cases, while Λ_{ZF} is almost temperature independent, a small yet clear increase in $\sigma_{ZF}(T)$ below T_c indicates the onset of spontaneous magnetic fields, thus representing the signature of TRS breaking in the superconducting state. For pure Re ($x = 0$), the results obtained using two different instruments (LTF and GPS) are highly consistent, further confirming the intrinsic nature of TRS breaking. On the other hand, upon further increasing the Mo content (i.e., $0.23 \leq x \leq 0.6$, see Supplementary Figs. 1, 2), the relaxation rates in the normal and the superconducting states become almost identical. Here, the lack of an additional relaxation below T_c implies a preserved TRS in the respective superconducting states (at least within the sensitivity of μSR). Further, longitudinal-field (LF) μSR measurements at base temperature, indicate that a field of only 15 mT (or 5 mT) is sufficient to fully decouple the muon spins from the weak spontaneous magnetic fields in pure Re (or in $Re_{0.88}Mo_{0.12}$), and that such weak internal fields are static within the muon lifetime. A comparison of ZF-μSR measurements, covering the whole $Re_{1-x}Mo_x$ phase diagram, shows that only the alloys with $x = 0$ and 0.12 exhibit a broken TRS in their superconducting states, while those with $0.23 \leq x \leq 0.60$, including here both the centrosymmetric- and non-centrosymmetric-$Re_{0.77}Mo_{0.23}$, preserve the TRS. The latter case, together with the preserved TRS in $Mg_{10}Ir_{19}B_{16}$, $Nb_{0.5}Os_{0.5}$, and Re_3W[17–19], all of which share the same α-Mn-type structure, implies that TRS breaking is clearly not related to the non-centrosymmetric crystal structure or to a possible mixed pairing but, most likely, is due to the presence of rhenium and to its amount. Indeed, in many ReTM alloys, if the Re-content is below a certain threshold, as, e.g., here in $Re_{1-x}Mo_x$ for high x (but also in Re_3W and Re_3Ta[19,27]), the TRS seems to be preserved.

On the other hand, it could also be that the spontaneous field is below the resolution of μSR technique in these samples. The use of other techniques, such as the optical Kerr effect[9], another very sensitive probe of spontaneous fields in unconventional superconductors, might clarify this issue.

Transverse field μSR and superconducting gap symmetry

To investigate the superconducting properties of the $Re_{1-x}Mo_x$, transverse-field (TF) μSR measurements were also performed across its phase diagram. The development of a flux-line lattice (FLL) in the mixed state of a superconductor broadens the internal field distribution, in turn reflected in an enhanced muon-spin depolarization rate. Since the latter is determined by the magnetic
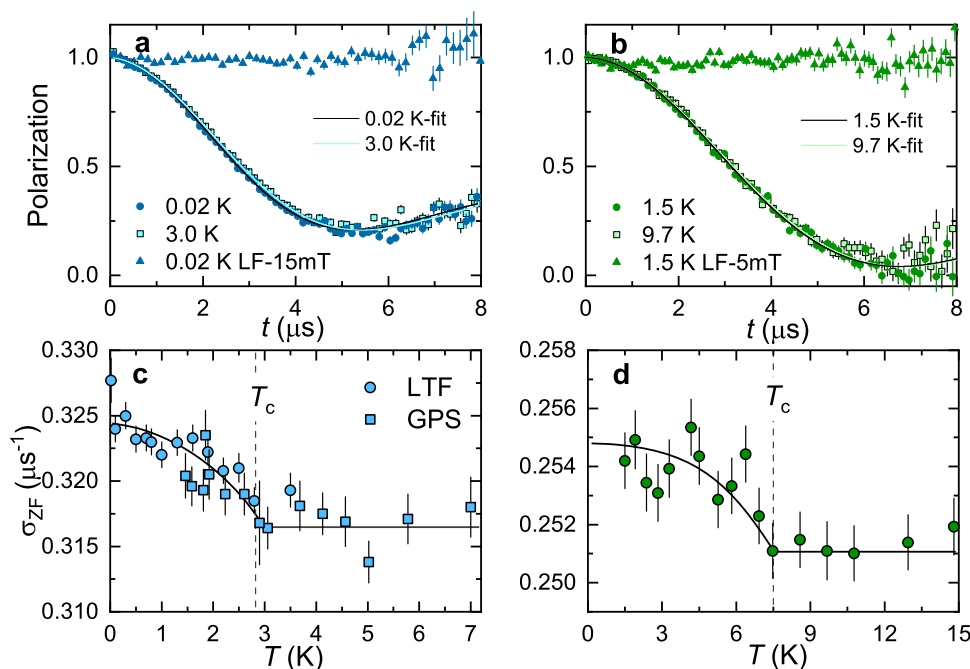
Fig. 2 ZF-μSR spectra bring evidence of TRS breaking. a, b ZF-μSR time spectra collected above and below T_c for Re$_{1-x}$Mo$_x$ alloys with $x = 0$ (**a**) and $x = 0.12$ (**b**). The ZF-μSR spectra of the other samples are shown in Supplementary Fig. 1. **c, d** Zero-field muon-spin relaxation rate versus temperature of Re$_{1-x}$Mo$_x$ with $x = 0$ (**c**) and $x = 0.12$ (**d**). A consistent increase of σ_{ZF} below T_c reflects the onset of spontaneous magnetic fields, indicative of a breaking of TRS in the superconducting state. The flat μSR datasets in **a** and **b** correspond to LF-μSR spectra, which suggest a prompt decoupling of the muon spins already at small LF. The solid lines through the data in **a** and **b** are fits to Eq. (1), while the solid lines in **c** and **d** are guides to the eyes. For $x = 0$, further ZF-μSR data were collected at the LTF spectrometer and shown to be highly consistent with the GPS datasets adopted from Shang et al.[14], where the data analysis is reported in great detail. The error bars of σ_{ZF} are the SDs obtained from fits to Eq. (1) by the `musrfit` software package[52].

penetration depth and, thus, by the superfluid density, the superconducting gap magnitude and symmetry can both be evaluated from the temperature-dependent superconducting relaxation rate (see Methods). The optimal field values for the TF-μSR measurements were identified from the lower critical field H_{c1} and the field dependence of the superconducting relaxation rate (see Supplementary Figs. 3, 4).

Following a field-cooling protocol, the TF-μSR spectra were collected at various temperatures upon warming up, covering both the superconducting and the normal states (see Fig. 3a to d). Below T_c, the fast decay induced by the FLL is clearly visible in all the samples. The slow decay in the normal state, instead, is attributed to the randomly oriented nuclear magnetic moments (similar to that of ZF-μSR in Fig. 2 and Supplementary Fig. 1) and expected to be the same also below T_c. The additional inhomogeneous field distribution caused by the FLL is clearly seen in the fast-Fourier-transform (FFT) spectra shown in Fig. 3e–h. Such field distribution could be modeled by means of Eq. (2).

The effective magnetic penetration depth and, in turn, the superfluid density were calculated from the measured Gaussian relaxation rates (see Methods). Figure 4 shows the inverse square of the effective magnetic penetration depth $\lambda_{eff}^{-2}(T)$ (proportional to the superfluid density) as a function of the reduced temperature (T/T_c) for the Re$_{1-x}$Mo$_x$ ($0 \le x \le 0.60$) alloys, covering all the four different phases. Although the Re$_{1-x}$Mo$_x$ alloys exhibit different T_c values and crystal structures (i.e., with or without an inversion center), below $T_c/3$, their λ_{eff}^{-2} values are practically independent of temperature. The low-T invariance of $\lambda_{eff}^{-2}(T)$ and, consequently, of the superfluid density, clearly suggests the lack of low-energy excitations and, hence, a fully gapped superconductivity in Re$_{1-x}$Mo$_x$, in good agreement with low-T electronic specific-heat measurements[20]. As shown by the solid lines in Fig. 4, $\lambda_{eff}^{-2}(T)$ is well-described by an s-wave model with a single superconducting gap. Both the clean- (Fig. 4) and dirty-limit

cases (Supplementary Fig. 10) produce similar results. The derived zero-temperature effective magnetic penetration depths λ_0, are comparable with the values calculated from the upper and lower critical fields (see Supplementary Table 1). In addition, also the superconducting-gap values are consistent with those derived from the specific-heat results[20].

DISCUSSION

First, we discuss why ReTM are fully-gapped superconductors. The lack of inversion symmetry in NCSCs often induces an antisymmetric spin-orbit coupling (ASOC), which splits the Fermi surface by lifting the degeneracy of the conduction-band electrons. As a consequence, both inter- and intraband Cooper pairs with the same or with opposite spin directions can be formed, thus allowing admixtures of spin-triplet and spin-singlet SC pairing. In general, the degree of such admixture is determined by the strength of ASOC and other microscopic parameters[1,10]. Yet, normally it is the ASOC to play the key role in the superconducting properties of NCSCs[1]. By increasing the strength of ASOC, a fully-gapped superconductor can be tuned into a nodal superconductor, the latter typically being dominated by the spin-triplet SC pairing. Such mechanism has been shown to occur, e.g., in Li$_2$(Pd,Pt)$_3$B[28,29] and, more recently, in CaPtAs[26,30]. As for ReTM NCSCs, despite the relatively large ASOC of rhenium atoms, all of them exhibit fully-gapped superconducting states, more consistent with singlet pairing[11–14,19,27]. However, we recall that often, due to the similar magnitude and same-sign of the order parameter on the spin-split Fermi surfaces, a possible mixed-pairing superconductor may be challenging to observe or to distinguish from a single-gap s-wave superconductor[31]. Considering that ReTM superconductors frequently exhibit TRS breaking below T_c, the existence of triplet pairing (and nodal superconductivity) is to be expected. For instance, both triplet-pairing
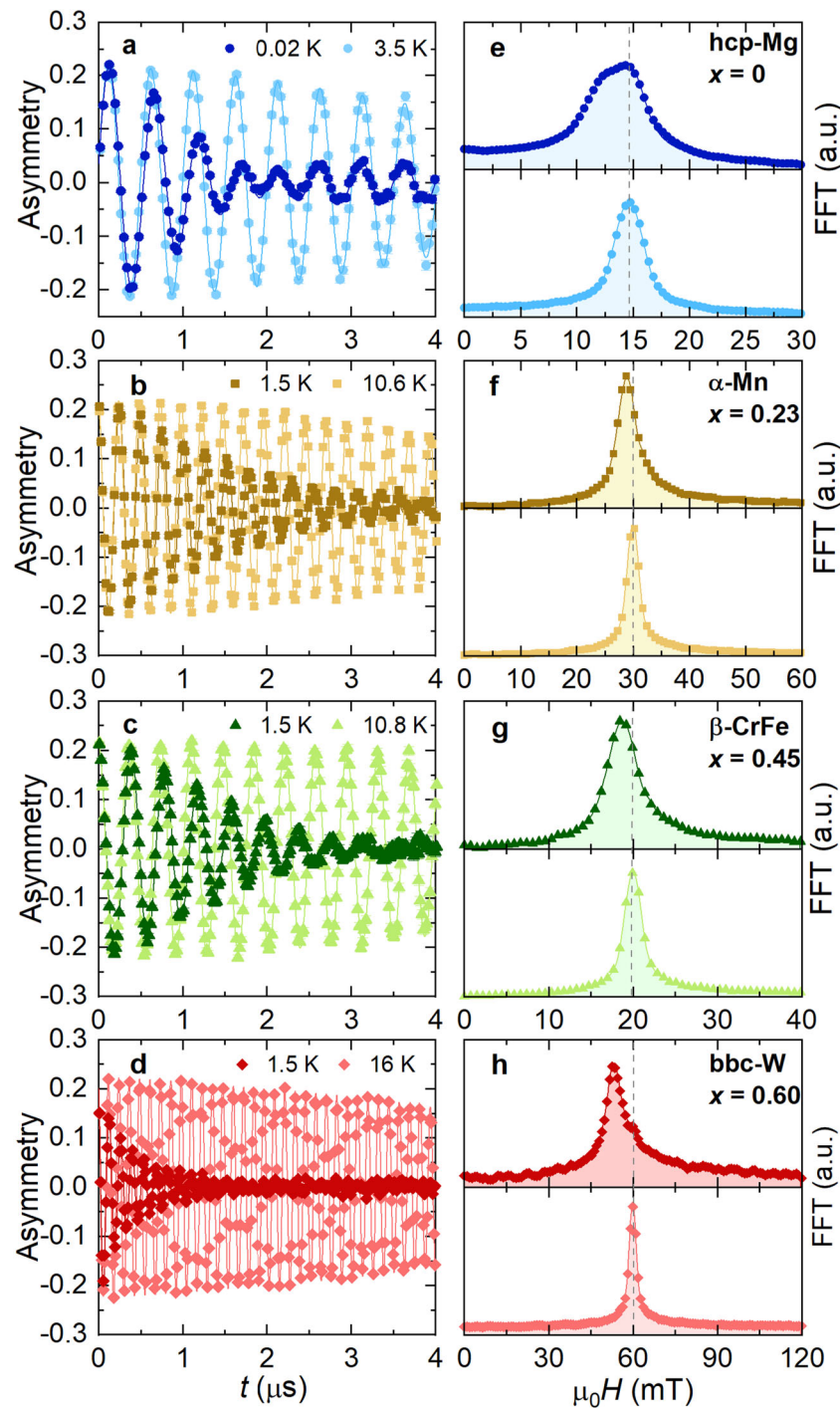
Fig. 3 Exploring $Re_{1-x}Mo_x$ superconductivity via TF-μSR. a, b, c, d TF-μSR time spectra, collected in the superconducting and in the normal state (i.e., below and above T_c), of different phases of $Re_{1-x}Mo_x$ alloys with $x = 0$ (hcp-Mg) (**a**), $x = 0.23$ (α-Mn) (**b**), $x = 0.45$ (β-CrFe) (**c**), and $x = 0.60$ (bcc-W) (**d**). **e, f, g, h** Fast Fourier transforms (FFT) of the time spectra shown in the left panels for $x = 0$ (**e**), $x = 0.23$ (**f**), $x = 0.45$ (**g**), and $x = 0.60$ (**h**). The upper and lower panels represent FFT in the superconducting and normal states, respectively. Clear diamagnetic shifts and field distribution broadening are observed in upper panels (superconducting state). The vertical dashed lines indicate the applied magnetic field in each case, always larger than the respective lower critical field value (see Supplementary Fig. 3 and Supplementary Table 1). Solid lines through the data are fits to Eq. (2). Panels **b** and **f** refer to the $x = 0.23$ (α-Mn) sample, synthesized via solid-state reaction. The sample prepared via arc melting exhibits similar features (see Supplementary Fig. 5). The temperature-dependent diamagnetic shifts are shown in Supplementary Fig. 6.

and TRS breaking superconductivity have been reported in Sr_2RuO_4, UPt_3, $LaNiGa_2$, and $LaNiC_2$[15,22,24,32–34], the latter representing a typical NCSC. In the α-Mn-type ReTM alloys, close to the Fermi level, the density of states (DOS) is dominated by the $5d$ orbitals of rhenium atoms, while contributions from the d orbitals

of TM are negligible[35,36]. Hence, even a significant increase in SOC —from $3d$ Ti to $4d$ Zr/Nb/Mo and to $5d$ Hf/Ta/W—is shown to not significantly affect the pairing admixture and thus the superconducting properties. Hence, in the ReTM family, the effect of
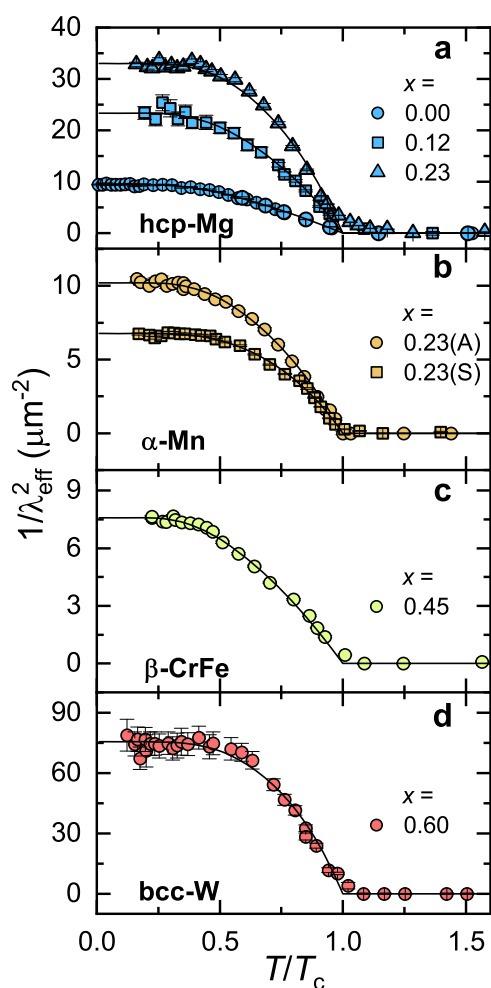
Fig. 4 Superfluid density and gap symmetry for different structures. a, b, c, d The superfluid density $[\rho_{sc}(T) \propto \lambda_{eff}^{-2}(T)]$ as a function of reduced temperature T/T_c for $Re_{1-x}Mo_x$ compounds with $x = 0$, 0.12, 0.23 (hcp-Mg) (**a**), $x = 0.23(S)$, 0.23(A) (α-Mn) (**b**), $x = 0.45$ (β-CrFe) (**c**), and $x = 0.60$ (bcc-W) (**d**). Lines through the data represent fits to a nodeless s-wave model in the clean limit (see Eq. (7)). The two datasets in **b** refer to the non-centrosymmetric α-Mn-type samples prepared by arc melting [0.23(A)] and solid state reaction [0.23(S)] methods. Similar fit results are obtained when using a dirty-limit model, as shown in Supplementary Fig. 10. The error bars of $\lambda_{eff}^{-2}(T)$ are the SDs obtained from the fits to Eq. (2) by the `musrfit` software package[52].

ASOC on admixtures of pairing remains elusive and requires additional work.

Unlike in the generic ReTM case, in the $Re_{1-x}Mo_x$ series considered here, the Re and Mo atoms occupy the same atomic positions of a centrosymmetric unit cell[20]. Hence, as the Mo content increases, the contribution of Mo $4d$ orbitals to the DOS is progressively enhanced, at the expense of the Re $5d$ orbitals. Naively, one would expect a progressive increase in singlet-pairing character as the Mo content increases. Yet, according to TF-μSR (Fig. 4) and zero-field specific-heat results[20], it seems that, despite a change in stoichiometry and of different crystal structures (both centro- and non-centrosymmetric) adopted by the $Re_{1-x}Mo_x$ alloys, they all behave as fully-gapped superconductors. This finding strongly suggests that, in the ReTM superconductors, spin-singlet pairing is dominant.

Second, we consider the role of rhenium in the time-reversal symmetry breaking. A dominating spin-singlet pairing in ReTM superconductors is clearly puzzling in view of the frequent occurrence of TRS breaking in this class of superconductors. As discussed above, the DOS is mostly determined by the Re $5d$ orbitals, since a replacement on the T-sites appears to have negligible effects on TRS breaking and on the superconducting pairing. At the same time, TRS is preserved in other Re-free α-Mn-type superconductors with similar SOC strength, as e.g., binary $Nb_{0.5}Os_{0.5}$ and ternary $Mg_{10}Ir_{19}B_{16}$[17,18,37]. The marginal role of SOC, together with the observation of broken TRS also in centrosymmetric elemental rhenium, strongly suggests that rhenium is crucial for understanding the broken TRS in the ReTM superconductors[14]. Considering that pure rhenium has a centrosymmetric crystal structure, the non-centrosymmetric crystal structure seems also inessential to TRS breaking in α-Mn-type Re-based superconductors. These indirect conclusions are clearly confirmed by our ZF-μSR measurements on $Re_{1-x}Mo_x$ ($0 \leq x \leq 0.60$) across the whole structural phase diagram.

The measurements we report here serve a dual purpose. Firstly, we extend previous $\sigma_{ZF}(T)$ results on elemental Re down to 0.02 K (originally limited to 1.5 K, although the T_c of Re is only 2.7 K). The current data (see Fig. 2c) are highly consistent with the previous ones[14] and exhibit a clear increase of $\sigma_{ZF}(T)$ near T_c, thus confirming that elemental rhenium breaks TRS in its superconducting state. Secondly, by systematically investigating the four different solid phases of $Re_{1-x}Mo_x$ ($0 \leq x \leq 0.60$) via ZF-μSR, we find that only those compounds close to the Re-rich side ($x \leq 0.12$, including elemental Re) show a superconducting state with broken TRS. In fact, for $x > 0.12$, although $Re_{1-x}Mo_x$ alloys exhibit various crystal structures (including the non-centrosymmetric α-Mn type), the TRS is preserved in the superconducting state, again implying that TRS breaking is not related to the lack of a center of symmetry, but rather to the presence of rhenium and to its content. Such conclusion is further reinforced by the preserved TRS in the extremely diluted Re-based superconductor, $ReBe_{22}$, whose Re-content is only 4%[38].

Finally, we discuss the relationship between TRS breaking and superconducting pairing. In general, this is a complex and still open question. Unconventional pairings, such as spin-triplet, are expected to break TRS in the superconducting state. For instance, Sr_2RuO_4 and UPt_3 exhibit both triplet superconductivity and broken TRS[39–42], the latter having been confirmed by ZF-μSR and Kerr effect[15,24,32,33]. Conversely, there are broken TRS states not involving triplet pairing, as e.g., the $s + id$ spin-singlet state proposed for some iron-based high-T_c superconducting materials[43]. In case of weak SOC, the internally-antisymmetric nonunitary triplet (INT) pairing can break the TRS, e.g., in centrosymmetric $LaNiGa_2$[34,44,45], and non-centrosymmetric $LaNiC_2$[22,46]. For such INT, the superconducting paring function is antisymmetric with respect to the orbital degree of freedom, while remaining symmetric in the spin- and crystal-momentum channels[22,34,44,46]. In Re-based superconductors, the point groups T_d and D_{6h}, relevant to α-Mn-type ReTM and hcp-Mg-type Re and $Re_{0.88}Mo_{0.12}$, respectively, have few irreducible representations whose dimension is larger than 1. In this case, an INT state can be achieved also in ReTM superconductors, where it can account for broken TRS in presence of a fully-opened gap, with either singlet-, triplet-, or admixed pairing. We recall that in ReTM superconductors, neither the TRS breaking nor the fully-gapped superconducting states are closely related to the structure symmetry, thus indicating that SOC is here inessential. Since SOC is ignored in INT pairing, this paradigm could provide a simple explanation of why a lack of inversion symmetry (essential to SOC) is not a precondition for TRS breaking in ReTM superconductors. Moreover, the occurrence of an INT state relies on the availability of a local-pairing mechanism driven by Hund's rules, e.g., by Ni d-electrons in $LaNiC_2$ and $LaNiGa_2$[22,34,44–46]. Since rhenium, too, can induce magnetism[47,48], such local-pairing mechanism may occur also in ReTM superconductors. In the latter case, TRS breaking would depend on Re

content but not on crystal structure, in agreement with the results we report here.

To conclude, in search of the origin of time-reversal symmetry breaking in Re-based superconductors, we performed comparative μSR studies in the $Re_{1-x}Mo_x$ family, covering all its four different solid phases: hcp-Mg, α-Mn, β-CrFe, and bcc-W, with α-Mn being non-centrosymmetric and the other three centrosymmetric. The superconductivity of $Re_{1-x}Mo_x$, including the lower and upper critical fields, was characterized by magnetization, electrical resistivity, and heat capacity measurements. The superfluid density at a microscopic level and the zero-field electronic specific heat at a macroscopic level both reveal a fully-gapped superconductivity in $Re_{1-x}Mo_x$. The spontaneous fields increase with decreasing temperature (below the onset of superconductivity), indicating that the superconducting states of centrosymmetric Re and $Re_{0.88}Mo_{0.12}$ break the TRS and are unconventional. By contrast, TRS is preserved in the $Re_{1-x}Mo_x$ compounds with a lower Recontent (i.e., $x \geq 0.23$), independent of their centro- or non-centrosymmetric crystal structures. Our findings on the $Re_{1-x}Mo_x$ family (here extended to two other superconducting phases, β-CrFe and bcc-W), together with those regarding other Re-free α-Mn-type superconductors, clearly imply that not only the Re presence, but also its amount are crucial for the appearance and the extent of TRS breaking in the ReTM superconductors. Further theoretical and experimental work is highly desirable to clarify the rhenium conundrum.

METHODS

Sample preparation

Polycrystalline $Re_{1-x}Mo_x$ alloys were prepared by arc melting Re (99.99%, ChemPUR) and Mo (99.95%, ChemPUR) powders with different stoichiometric ratios in a high-purity argon atmosphere. To improve the homogeneity, samples were flipped and remelted several times and, some of the as-cast ingots, e.g., hcp-Mg- and bcc-W-type, were annealed at 900°C for two weeks. The clean β-CrFe phase (e.g., $Re_{0.55}Mo_{0.45}$) was obtained by interrupting the heating immediately after the melting of the precursors, similar to a quench process. Hence, all the measurements reported here for the β-CrFe-type samples refer to as-cast samples. The α-Mn-type samples with a non-centrosymmetric crystal structure (e.g, $Re_{0.77}Mo_{0.23}$) were synthesized by both arc melting and solid-state reaction methods. The arc-melted sample, which shows a majority of hcp-Mg phase, was annealed over one week at 1400 °C in a mixed argon/hydrogen (95%/5%) atmosphere to stabilize the α-Mn phase. Such phase could also be obtained by annealing the mixture of Re and Mo powders at 1400 °C in argon/hydrogen atmosphere over one week.

Lower- and upper critical fields

The lower critical field H_{c1} was determined by field-dependent magnetization measurements at various temperatures up to T_c, while the upper critical field H_{c2} was determined by measuring the temperature-dependent electrical resistivity and heat capacity under various magnetic fields, and by field-dependent magnetization at various temperatures. The magnetization, electrical resistivity, and heat capacity measurements were performed on a Quantum Design magnetic property measurement system (MPMS) and a physical property measurement system (PPMS). The details of zero-field electrical resistivity and heat capacity results, as well as the low-field magnetic susceptibility data are reported in a previous study (see Shang et al.[20]).

The results of the lower critical field measurements for $Re_{1-x}Mo_x$ ($0.12 \leq x \leq 0.60$) are summarized in Supplementary Fig. 3. The estimated $\mu_0H_{c1}(0)$ values are listed in the right panel of Supplementary Fig. 3 and in Supplementary Table 1. The $\mu_0H_{c1}(0)$ of pure Re (hcp-Mg) can be found in Shang et al.[14]. The results of the upper critical fields H_{c2} for $Re_{1-x}Mo_x$ ($0 \leq x \leq 0.60$) are presented in Supplementary Figs. 7, 9. The $\mu_0H_{c2}(T)$ data were analyzed by both Werthamer–Helfand–Hohenberg (WHH) and Ginzburg–Landau (GL) models[49,50]. The estimated $\mu_0H_{c2}(0)$ values are also listed in Supplementary Table 1. The coherence length $\xi(0)$ was calculated from $\xi(0) = \sqrt{\Phi_0/2\pi H_{c2}(0)}$, where $\Phi_0 = 2.07 \times 10^{-3}$ T μm^2 is the quantum of magnetic flux. The GL magnetic penetration depth λ_{GL} is related to the coherence length and the lower critical field via $\mu_0H_{c1} = (\Phi_0/4\pi\lambda_{GL}^2)[\ln(\kappa) + 0.5]$, where $\kappa = \lambda_{GL}/\xi$ is the GL parameter[51]. By using $\mu_0H_{c1}(0)$ and $\xi(0)$ calculated from $\mu_0H_{c2}(0)$, the GL magnetic penetration depths $\lambda_{GL}(0)$ could be determined. They too are listed in Supplementary Table. 1 and are fully consistent with the experimental values from TF-μSR data. The GL parameter κ for $Re_{1-x}Mo_x$ ($0 \leq x \leq 0.60$) (see Supplementary Table 1), is always much larger than the threshold value $1/\sqrt{2}$, thus clearly confirming that all $Re_{1-x}Mo_x$ alloys are type-II superconductors.

μSR experiments

The μSR experiments were conducted at the general-purpose surface-muon (GPS) and at the low-temperature facility (LTF) instruments of the Swiss muon source (SμS) at Paul Scherrer Institut (PSI) in Villigen, Switzerland. Once implanted in a material, typically within ~0.1 mm, spin-polarized muons act as microscopic probes of the local magnetic environment via the decay positrons, emitted preferentially along the muon-spin direction. The spatial anisotropy of the emitted positrons (i.e., the asymmetry signal) reveals the distribution of the local magnetic fields at the muon stopping sites. For ZF-μSR measurements, to exclude the possibility of stray magnetic fields, the magnets were quenched before starting the measurements, and an active field-nulling facility was used to compensate for stray fields down to 1 μT. In both the TF- and LF-μSR cases, the samples were cooled in an applied magnetic field down to the base temperature (1.5 K for GPS and 0.02 K for LTF). The μSR spectra were then collected upon heating.

Analysis of the ZF-μSR data

All the μSR data were analyzed by means of the `musrfit` software package[52]. Due to the non-magnetic nature of $Re_{1-x}Mo_x$, in the absence of applied external fields, the relaxation is mainly determined by the randomly oriented nuclear moments. Therefore, the ZF-μSR spectra can be modeled by means of a phenomenological relaxation function, consisting of a combination of Gaussian- and Lorentzian Kubo-Toyabe relaxations[53,54]:

$$A_{ZF} = A_s \left[\frac{1}{3} + \frac{2}{3}(1 - \sigma_{ZF}^2 t^2 - \Lambda_{ZF}t)\, e^{\left(-\frac{\sigma_{ZF}^2 t^2}{2} - \Lambda_{ZF}t\right)} \right] + A_{bg}. \quad (1)$$

Here A_s and A_{bg} represent the initial muon-spin asymmetries for muons implanted in the sample and the sample holder, respectively. The muon-spin polarization, reported in the top row of Fig. 2, is the total initial asymmetry A_{ZF} normalized to its $t = 0$ value. In polycrystalline samples, the 1/3-non-relaxing and 2/3-relaxing components of the asymmetry correspond to the powder average of the local internal field with respect to the initial muon-spin orientation. The σ_{ZF} and Λ_{ZF} represent the zero-field Gaussian and Lorentzian relaxation rates, respectively. Since Λ_{ZF} shows an almost temperature-independent behavior, the σ_{ZF} values in Fig. 2c and d could be derived by fixing Λ_{ZF} to its average value, here, $\Lambda_{ZF} = 0.0144$ ($x = 0$) and $0.005 \mu s^{-1}$ ($x = 0.12$). Further details about the data analysis can also be found in Shang et al.[14].

Analysis of the TF-μSR data

In the TF-μSR case, the time evolution of the asymmetry can be modeled by:

$$A_{TF}(t) = \sum_{i=1}^{n} A_i \cos(\gamma_\mu B_i t + \phi)e^{-\sigma_i^2 t^2/2} + A_{bg}\cos(\gamma_\mu B_{bg}t + \phi). \quad (2)$$

Here A_i and A_{bg} are the same as in ZF-μSR. B_i and B_{bg} are the local fields sensed by implanted muons in the sample and the sample holder, γ_μ is the muon gyromagnetic ratio, ϕ is the shared initial phase, and σ_i is the Gaussian relaxation rate of the ith component. The number of the required components depends on the field distribution in the mixed superconducting state, here we found $1 \leq n \leq 3$ for $Re_{1-x}Mo_x$. In case of multi-component oscillations, the first term in Eq. (2) describes the field distribution as the sum of n Gaussian relaxations[55]:

$$p(B) = \gamma_\mu \sum_{i=1}^{n} \frac{A_i}{\sigma_i} \exp\left(-\frac{\gamma_\mu^2(B - B_i)^2}{2\sigma_i^2}\right). \quad (3)$$

The first- and the second moments of the field distribution in the sample

can be calculated by:

$$\langle B \rangle = \sum_{i=1}^{n} \frac{A_i B_i}{A_{tot}}, \tag{4}$$

and

$$\langle B^2 \rangle = \frac{\sigma_{eff}^2}{\gamma_\mu^2} = \sum_{i=1}^{n} \frac{A_i}{A_{tot}} \left[\frac{\sigma_i^2}{\gamma_\mu^2} + (B_i - \langle B \rangle)^2 \right], \tag{5}$$

where $A_{tot} = \sum_{i=1}^{n} A_i$. The total Gaussian relaxation rate σ_{eff} in Eq. (5) includes contributions from both a temperature-independent relaxation, due to nuclear moments (σ_n, similar to σ_{ZF}), and a temperature-dependent relaxation, related to the flux-line lattice (σ_{sc}) in the superconducting state. The σ_{sc} values were extracted by subtracting the nuclear contribution following $\sigma_{sc} = \sqrt{\sigma_{eff}^2 - \sigma_n^2}$.

Extracting the superconducting gap and its symmetry from TF-μSR data

Since σ_{sc} is directly related to the effective magnetic penetration depth and thus to the superfluid density ($\sigma_{sc} \propto 1/\lambda_{eff}^2 \sim \rho_{sc}$), the superconducting gap and its symmetry can be investigated by measuring the temperature-dependent σ_{sc}. For small applied magnetic fields [$H_{appl}/H_{c2} \ll 1$], the effective magnetic penetration depth λ_{eff} can be calculated from the measured σ_{sc}[51,56]:

$$\frac{\sigma_{sc}^2(T)}{\gamma_\mu^2} = 0.00371 \frac{\Phi_0^2}{\lambda_{eff}^4(T)}. \tag{6}$$

For Re$_{1-x}$Mo$_x$ ($0 \leq x \leq 0.60$), the H_{appl}/H_{c2} ratios are comprised between 0.23% and 2.6% (see Supplementary Table 1), hence justifying the use of the above equation. To extract the superconducting gap and its symmetry, the temperature-dependent superfluid density $\rho_{sc}(T)$ [$\propto \lambda_{eff}^{-2}(T)$] of Re$_{1-x}Mo_x$ was analyzed by using a fully gapped s-wave model, generally described by:

$$\rho_{sc}(T) = \frac{\lambda_0^2}{\lambda_{eff}^2(T)} = 1 + 2 \int_{\Delta(T)}^{\infty} \frac{E}{\sqrt{E^2 - \Delta^2(T)}} \frac{\partial f}{\partial E} dE, \tag{7}$$

where $f = (1 + e^{E/k_B T})^{-1}$ is the Fermi function[57,58], λ_0 is the effective magnetic penetration depth at zero temperature. The temperature dependence of the gap value is given by $\Delta(T) = \Delta_0 \tanh\{1.82[1.018(T_c/T - 1)]^{0.51}\}$[59], where Δ_0 is the gap value at zero temperature.

Unlike in the clean-limit case [see Eq. (7)], in the dirty limit, the coherence length ξ_0 is larger than the electronic mean-free path l_e. In this case, in the BCS approximation, the temperature dependence of the superfluid density is given by[57]:

$$\rho_{sc}(T) = \frac{\lambda_0^2}{\lambda_{eff}^2(T)} = \frac{\Delta(T)}{\Delta_0} \tanh\left[\frac{\Delta(T)}{2k_B T}\right]. \tag{8}$$

For Re$_{1-x}$Mo$_x$ ($0 \leq x \leq 0.60$), ξ_0 and l_e exhibit similar magnitudes. Hence, in this case, both Eqs. (7) and (8) describe very well the low-T superfluid density, and yield similar superconducting gap values (see Supplementary Table 1).

DATA AVAILABILITY

All the data needed to evaluate the reported conclusions are presented in the paper and/or in the Supplementary Materials. Additional data related to this paper may be requested from the authors. The μSR data were generated at the SμS (Paul Scherrer Institut, Switzerland). Derived data supporting the results of this study are available from the corresponding authors or beamline scientists. The musrfit software package is available online free of charge at http://lmu.web.psi.ch/musrfit/technical/index.html.

REFERENCES
1. Bauer, E., Sigrist, M., eds., *Non-Centrosymmetric Superconductors*, vol. 847 (Springer Verlag, Berlin, 2012).
2. Kim, H. et al. Beyond triplet: unconventional superconductivity in a spin-3/2 topological semimetal. *Sci. Adv.* **4**, eaao4513 (2018).
3. Sun, Z. X. et al. Dirac surface states and nature of superconductivity in non-centrosymmetric BiPd. *Nat. Commun.* **6**, 6633 (2015).
4. Ali, M. N., Gibson, Q. D., Klimczuk, T. & Cava, R. J. Noncentrosymmetric super-conductor with a bulk three-dimensional Dirac cone gapped by strong spin-orbit coupling. *Phys. Rev. B* **89**, 020505 (2014).
5. Sato, M. & Fujimoto, S. Topological phases of noncentrosymmetric super-conductors: edge states, Majorana fermions, and non-Abelian statistics. *Phys. Rev. B* **79**, 094504 (2009).
6. Tanaka, Y., Mizuno, Y., Yokoyama, T., Yada, K. & Sato, M. Anomalous Andreev bound state in noncentrosymmetric superconductors. *Phys. Rev. Lett.* **105**, 097002 (2010).
7. Sato, M. & Ando, Y. Topological superconductors: a review. *Rep. Prog. Phys.* **80**, 076501 (2017).
8. Qi, X.-L. & Zhang, S.-C. Topological insulators and superconductors. *Rev. Mod. Phys.* **83**, 1057–1110 (2011).
9. Kallin, C. & Berlinsky, J. Chiral superconductors. *Rep. Prog. Phys.* **79**, 054502 (2016).
10. Smidman, M., Salamon, M. B., Yuan, H. Q. & Agterberg, D. F. Superconductivity and spin-orbit coupling in non-centrosymmetric materials: a review. *Rep. Prog. Phys.* **80**, 036501 (2017).
11. Singh, R. P. et al. Detection of time-reversal symmetry breaking in the non-centrosymmetric superconductor Re$_6$Zr using muon-spin spectroscopy. *Phys. Rev. Lett.* **112**, 107002 (2014).
12. Singh, D. et al. Time-reversal symmetry breaking in the noncentrosymmetric superconductor Re$_6$Hf: further evidence for unconventional behavior in the α-Mn family of materials. *Phys. Rev. B* **96**, 180501 (2017).
13. Shang, T. et al. Nodeless superconductivity and time-reversal symmetry breaking in the noncentrosymmetric superconductor Re$_{24}$Ti$_5$. *Phys. Rev. B* **97**, 020502 (2018).
14. Shang, T. et al. Time-reversal symmetry breaking in Re-based superconductors. *Phys. Rev. Lett.* **121**, 257002 (2018).
15. Luke, G. M. et al. Time-reversal symmetry-breaking superconductivity in Sr$_2$RuO$_4$. *Nature* **394**, 558–561 (1998).
16. Aoki, Y. et al. Time-reversal symmetry-breaking superconductivity in heavy-fermion PrOs$_4$Sb$_{12}$ detected by muon-spin relaxation. *Phys. Rev. Lett.* **91**, 067003 (2003).
17. Aczel, A. A. et al. Muon spin rotation/relaxation measurements of the non-centrosymmetric superconductor Mg$_{10}$Ir$_{19}$B$_{16}$. *Phys. Rev. B* **82**, 024520 (2010).
18. Singh, D. et al. Superconducting properties and μSR study of the non-centrosymmetric superconductor Nb$_{0.5}$Os$_{0.5}$. *J. Phys.: Condens. Matter* **30**, 075601 (2018).
19. Biswas, P. K., Hillier, A. D., Lees, M. R. & Paul, D. M. Comparative study of the centrosymmetric and noncentrosymmetric superconducting phases of Re$_3$W using muon spin spectroscopy and heat capacity measurements. *Phys. Rev. B* **85**, 134505 (2012).
20. Shang, T. et al. Structure and superconductivity in the binary Re$_{1-x}$Mo$_x$ alloys. *Phys. Rev. Mater.* **3**, 024801 (2019).
21. Amato, A. Heavy-fermion systems studied by μSR technique. *Rev. Mod. Phys.* **69**, 1119–1180 (1997).
22. Hillier, A. D., Quintanilla, J. & Cywinski, R. Evidence for time-reversal symmetry breaking in the noncentrosymmetric superconductor LaNiC$_2$. *Phys. Rev. Lett.* **102**, 117007 (2009).
23. Barker, J. A. T. et al. Unconventional superconductivity in La$_7$Ir$_3$ revealed by muon spin relaxation: Introducing a new family of noncentrosymmetric superconductor that breaks time-reversal symmetry. *Phys. Rev. Lett.* **115**, 267001 (2015).
24. Luke, G. M. et al. Muon spin relaxation in UPt$_3$. *Phys. Rev. Lett.* **71**, 1466–1469 (1993).
25. Shang, T. et al. Time-reversal symmetry breaking in the noncentrosymmetric Zr$_3$Ir superconductor. *Phys. Rev. B* **102**, 020503 (2020).
26. Shang, T. et al. Simultaneous nodal superconductivity and time-reversal symmetry breaking in the noncentrosymmetric superconductor CaPtAs. *Phys. Rev. Lett.* **124**, 207001 (2020).
27. Barker, J. A. T. et al. Superconducting and normal-state properties of the non-centrosymmetric superconductor Re$_3$Ta. *Phys. Rev. B* **98**, 104506 (2018).
28. Yuan, H. Q. et al. S-wave spin-triplet order in superconductors without inversion symmetry: Li$_2$Pd$_3$B and Li$_2$Pt$_3$B. *Phys. Rev. Lett.* **97**, 017006 (2006).
29. Nishiyama, M., Inada, Y. & Zheng, G.-q Spin triplet superconducting state due to broken inversion symmetry in Li$_2$Pt$_3$B. *Phys. Rev. Lett.* **98**, 047002 (2007).
30. Xie, W. et al. CaPtAs: a new noncentrosymmetric superconductor. *Sci. China-Phys. Mech. Astron.* **63**, 237412 (2020).
31. Yip, S. Noncentrosymmetric superconductors. *Annu. Rev. Condens. Matter Phys.* **5**, 15–33 (2014).
32. Xia, J., Maeno, Y., Beyersdorf, P. T., Fejer, M. M. & Kapitulnik, A. High resolution polar Kerr effect measurements of Sr$_2$RuO$_4$: evidence for broken time-reversal symmetry in the superconducting state. *Phys. Rev. Lett.* **97**, 167002 (2006).

33. Schemm, E. R., Gannon, W. J., Wishne, C. M., Halperin, W. P. & Kapitulnik, A. Observation of broken time-reversal symmetry in the heavy-fermion superconductor UPt$_3$. *Science* **345**, 190–193 (2014).

34. Hillier, A. D., Quintanilla, J., Mazidian, B., Annett, J. F. & Cywinski, R. Nonunitary triplet pairing in the centrosymmetric superconductor LaNiGa$_2$. *Phys. Rev. Lett.* **109**, 097001 (2012).

35. Winiarski, M. J. Electronic structure of non-centrosymmetric superconductors Re$_{24}$(Nb;Ti)$_5$ by *ab initio* calculations. *J. Alloy. Compd.* **616**, 1–4 (2014).

36. Mojammel, A. K. et al. Complex superconductivity in the noncentrosymmetric compound Re$_6$Zr. *Phys. Rev. B* **94**, 144515 (2016).

37. Singh, D., K. P., S., Marik, S., Hillier, A. D. & Singh, R. P. Superconducting and normal state properties of the noncentrosymmetric superconductor NbOs$_2$ investigated by muon spin relaxation and rotation. *Phys. Rev. B* **99**, 014516 (2019).

38. Shang, T. et al. Enhanced T_c and multiband superconductivity in the fully-gapped ReBe$_{22}$ superconductor. *New J. Phys.* **21**, 073034 (2019).

39. Ishida, K. et al. Spin-triplet superconductivity in Sr$_2$RuO$_4$ identified by ^{17}O Knight shift. *Nature* **396**, 658–660 (1998).

40. Tou, H. et al. Nonunitary spin-triplet superconductivity in UPt$_3$: evidence from ^{195}Pt Knight shift study. *Phys. Rev. Lett.* **80**, 3129–3132 (1998).

41. Mackenzie, A. P. & Maeno, Y. The superconductivity of Sr$_2$RuO$_4$ and the physics of spin-triplet pairing. *Rev. Mod. Phys.* **75**, 657–712 (2003).

42. Joynt, R. & Taillefer, L. The superconducting phases of UPt$_3$. *Rev. Mod. Phys.* **74**, 235–294 (2002).

43. Lee, W.-C., Zhang, S.-C. & Wu, C. Pairing state with a time-reversal symmetry breaking in FeAs-based superconductors. *Phys. Rev. Lett.* **102**, 217002 (2009).

44. Weng, Z. F. et al. Two-gap superconductivity in LaNiGa$_2$ with nonunitary triplet pairing and even parity gap symmetry. *Phys. Rev. Lett.* **117**, 027001 (2016).

45. Ghosh, S. K. et al. Quantitative theory of triplet pairing in the unconventional superconductor LaNiGa$_2$. *Phys. Rev. B* **101**, 100506 (2020).

46. Quintanilla, J., Hillier, A. D., Annett, J. F. & Cywinski, R. Relativistic analysis of the pairing symmetry of the noncentrosymmetric superconductor LaNiC$_2$. *Phys. Rev. B* **82**, 174511 (2010).

47. Yang, S. et al. Tuning the optical, magnetic, and electrical properties of ReSe$_2$ by nanoscale strain engineering. *Nano Lett.* **15**, 1660–1666 (2015).

48. Kochat, V. et al. Re doping in 2D transition metal dichalcogenides as a new route to tailor structural phases and induced magnetism. *Adv. Mater.* **29**, 1703754 (2017).

49. Werthamer, N. R., Helfand, E. & Hohenberg, P. C. Temperature and purity dependence of the superconducting critical field, H_{c2}. III. Electron spin and spin-orbit effects. *Phys. Rev.* **147**, 295–302 (1966).

50. Zhu, X., Yang, H., Fang, L., Mu, G. & Wen, H.-H. Upper critical field, Hall effect and magnetoresistance in the iron-based layered superconductor LaFeAsO$_{0.9}$F$_{0.1-\delta}$. *Supercond. Sci. Technol.* **21**, 105001 (2008).

51. Brandt, E. H. Properties of the ideal Ginzburg-Landau vortex lattice. *Phys. Rev. B* **68**, 054506 (2003).

52. Suter, A. & Wojek, B. M. Musrfit: A free platform-independent framework for μSR data analysis. *Phys. Procedia* **30**, 69–73 (2012).

53. Kubo, R., Toyabe, T., A stochastic model for low-field resonance and relaxation. In Blinc, R., ed., Magnetic Resonance and Relaxation. Proceedings of the XIVth Colloque Ampère, 810–823 (North-Holland, Amsterdam, 1967).

54. Yaouanc, A. & de Réotier, P. D. *Muon Spin Rotation, Relaxation, and Resonance: Applications to Condensed Matter*. (Oxford University Press, Oxford, 2011).

55. Maisuradze, A., Khasanov, R., Shengelaya, A. & Keller, H. Comparison of different methods for analyzing μSR line shapes in the vortex state of type-II superconductors. *J. Phys.: Condens. Matter.* **21**, 075701 (2009).

56. Barford, W. & Gunn, J. M. F. The theory of the measurement of the London penetration depth in uniaxial type II superconductors by muon spin rotation. *Physica C* **156**, 515–522 (1988).

57. Tinkham, M., *Introduction to Superconductivity*. 2nd ed. (Dover Publications, Mineola, NY, 1996).

58. Prozorov, R. & Giannetta, R. W. Magnetic penetration depth in unconventional superconductors. *Supercond. Sci. Technol.* **19**, R41–R67 (2006).

59. Carrington, A. & Manzano, F. Magnetic penetration depth of MgB$_2$. *Physica C* **385**, 205–214 (2003).

AUTHOR CONTRIBUTIONS

T.S., T.Sh., and M.S. conceived and led the project. T.S., D.J.G., and E.P. synthesized the samples. T.S., T.Sh., and C.B. performed the μSR measurements. T.S., M. M., and L.J.C. measured the electrical resistivity, heat capacity, and magnetization. T.S. and T.Sh. analyzed all the experimental data. T.S. and T.Sh. wrote the paper with input from all the authors.

COMPETING INTERESTS

The authors declare no competing interests.

ADDITIONAL INFORMATION

Supplementary information is available for this paper at https://doi.org/10.1038/s41535-020-00279-1.

Correspondence and requests for materials should be addressed to T.S. or T.S.

Reprints and permission information is available at http://www.nature.com/reprints

Publisher's note Springer Nature remains neutral with regard to jurisdictional claims in published maps and institutional affiliations.